

# Temperature-Dependent Terahertz Emission from Co/Mn<sub>2</sub>Au Spintronic Bilayers

Yangyang Ni, Zuanming Jin,\* Bangju Song, Xiaofeng Zhou, Haiyang Chen, Cheng Song,\* Yan Peng, Chao Zhang, Feng Pan, Guohong Ma, Yiming Zhu,\* and Songlin Zhuang

Recently, ferromagnetic/nonmagnetic heavy metal heterostructures have been intensively investigated as terahertz (THz) emitters. The interconversion of spin-to-charge dynamics plays a central role for efficient emission of THz electromagnetic pulses. However, a direct observation of spin–charge interconversion in antiferromagnetic (AFM) materials occurring on the sub-picosecond time scale remains a challenge. Herein, the magnetic-field-, pump-fluence-, and polarization-dependent THz emission behaviors by a femtosecond optical pump in cobalt (Co)/Mn<sub>2</sub>Au nanometer heterostructure are experimentally investigated. The Co/Mn<sub>2</sub>Au bilayer generates sizable THz signals, whereas the Mn<sub>2</sub>Au/Pt bilayer does not show any THz emission. In addition, the thickness- and temperature-dependent THz emission measurements indicate a direct relation between the THz amplitude and the conductivity of AFM Mn<sub>2</sub>Au layer. The results obtained will not only promote the fundamental understanding of ultrafast spin–charge interconversion in Co/Mn<sub>2</sub>Au heterostructures, but also provide a possibility of spectroscopic-based spin current detector at THz-frequency range.

phenomenon is the magnon resonance in AFM materials, which can be induced by THz Zeeman torque,<sup>[4]</sup> optical Raman-type excitation,<sup>[5]</sup> and electric dipole-mediated nonlinear THz-spin coupling.<sup>[6]</sup> Recently, coherent spin pumping effects have been observed in AFM/Pt heterostructure.<sup>[7,8]</sup> THz radiation pumps spin currents into adjacent metals, which convert into charge currents through inverse spin-Hall effect (ISHE)<sup>[9]</sup> and results in an open-circuit DC voltage. In contrast, an optical generation of ultrafast spin current was reported in the NiO (20 nm)/Pt (3 nm).<sup>[10]</sup> Although the pure spin current has been demonstrated via ultrafast spin pumping,<sup>[11,12]</sup> the readout of the spin information in AFM is still difficult as they are generally not sensitive to the external field, as the net magnetization of AFM is much smaller than that of ferromagnetic (FM) materials.

## 1. Introduction

Due to the terahertz (THz) spin dynamics and absence of the net magnetization, antiferromagnetic (AFM) materials offer unique advantages for ultrafast and diverse spin-based nanoscale device functionalities.<sup>[1–3]</sup> The most widely studied physical

It is worth noting that all-electrical switching of the magnetization in AFM materials with lacking of the local inversion symmetry has attracted tremendous interests, which is critical for potential applications of AFM spintronics.<sup>[13–17]</sup> In the case of conductive bimetallic alloys containing Mn, a large anomalous Hall effect (AHE) and spin Hall effect (SHE) have been

Y. Ni, Z. Jin, Y. Peng, Y. Zhu, S. Zhuang  
Shanghai Key Lab of Modern Optical System, and Engineering Research Center of Optical Instrument and System (Ministry of Education)  
University of Shanghai for Science and Technology  
516 JunGong Road, Shanghai 200093, China  
E-mail: physics\_jzm@usst.edu.cn; ymzhu@usst.edu.cn

B. Song, H. Chen, G. Ma  
Department of Physics  
Shanghai University  
99 Shangda Road, Shanghai 200444, P. R. China


X. Zhou, C. Song, F. Pan  
Key Laboratory of Advanced Materials, School of Materials Science and Engineering  
Tsinghua University  
Beijing 100084, China  
E-mail: songcheng@mail.tsinghua.edu.cn

C. Zhang  
School of Physics  
University of Wollongong  
Wollongong, New South Wales 2522, Australia

G. Ma  
SIOM & STU Joint Laboratory for Superintense Lasers and the Applications  
Shanghai 201210, China

Z. Jin, Y. Peng, Y. Zhu, S. Zhuang  
Shanghai Institute of Intelligent Science and Technology  
Tongji University  
1239 Siping Road, Shanghai 200092, P. R. China

Y. Zhu  
Shanghai International Travel Health Care Center (Shanghai Customs Port Clinic)

 The ORCID identification number(s) for the author(s) of this article can be found under <https://doi.org/10.1002/pssr.202100290>.

DOI: 10.1002/pssr.202100290

theoretically proposed, due to the large spin-orbit coupling of heavy atoms and the Berry phase of the noncollinear spin textures.<sup>[18,19]</sup> In contrast to insulating AFM materials, magneto-optical Kerr effect in the Mn<sub>3</sub>Rh, Mn<sub>3</sub>Ir, and Mn<sub>3</sub>Pt can be attributed to the nontrivial off-diagonal optical conductivity.<sup>[20]</sup> Due to the high Néel temperature, the mechanical hardness, and resistant to oxidation, metallic AFM materials have been considered as promising candidates for the exchange bias layer in spin valves,<sup>[21,22]</sup> the magnetoresistance in nonvolatile memories,<sup>[23]</sup> and the tips of scanning tunneling microscopy.<sup>[24]</sup>

The deep understanding of dynamical generation and detection of ultrafast spin currents is not only of fundamental interest in conductive AFM spintronics, but also of practical relevance for THz photonic applications.<sup>[25,26]</sup> To date, what has been measured in bilayers of YIG/Ir<sub>20</sub>Mn<sub>80</sub><sup>[27]</sup> and YIG/Mn<sub>2</sub>Au<sup>[28]</sup> is that the steady-state spin currents accumulation in the heterostructures, detected by sensing peaks or dips in the DC voltage. Nevertheless, the electrical measurements require microstructuring of the samples, which is costly, time consuming, and may complicate data interpretation due to additional electric contacting. In addition, the microwave rectification and heating-related thermoelectric electromotive force are unavoidable in the microwave spin pumping effect<sup>[29]</sup> and spin Seebeck effect<sup>[30]</sup> measurements, respectively. A crucial missing is a direct experimental observation of ultrafast spin-charge conversion of AFM within the THz-frequency range, although it has been widely investigated in paramagnetic heavy metals,<sup>[31–34]</sup> 2D MoS<sub>2</sub>,<sup>[35]</sup> and topological insulators of Bi<sub>2</sub>Se<sub>3</sub> and Bi<sub>2</sub>Te<sub>3</sub>.<sup>[36–38]</sup>

In this work, we use ultrafast laser pumping-induced THz emission, as a method to investigate the ultrafast spin-charge conversion in Co/Mn<sub>2</sub>Au bilayer on a femtosecond timescale. A series of experiments have been carried out to reveal that laser-induced spin transport plays a dominant role in the THz emission from Co/Mn<sub>2</sub>Au nanofilms. We study the temperature dependence of the THz emission from 10 K to room temperature. A continuous decrease is observed as temperature decreasing, which is opposite to the temperature-dependent magnetization of Co/Mn<sub>2</sub>Au. By analyzing different contributions, we found the conductivity of Mn<sub>2</sub>Au plays a dominant role at low temperature, probed by THz transients. The insights into the mechanisms underlying the THz generation in FM/AFM are crucial for developing THz photonic-based rapid screening of AFM materials in terms of spin-to-charge conversion.

## 2. Results and Discussion

The schematic of THz emission experiment is shown in **Figure 1a**. Fabricated by magnetron sputtering, 5 or 8 nm metallic Mn<sub>2</sub>Au layer on the single crystal MgO (100) substrate was capped with the 3 nm Co film. The MgO substrate thickness is 500 μm. To avoid oxidation of the sample, the bilayer sample was covered by 1.5 nm Al, which oxidizes in ambient atmosphere and serves as a capping layer (see Experimental Section). The linearly polarized ultrashort optical beam (center wavelength, 800 nm; repetition rate, 1 kHz; pulse duration, 120 fs) was

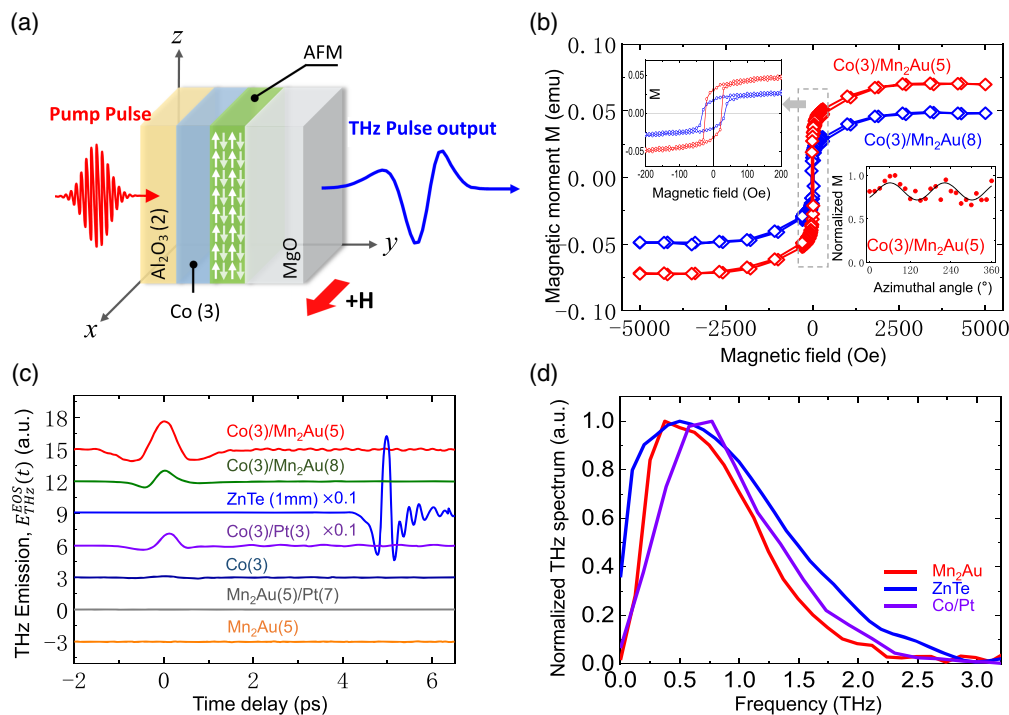


**Figure 1.** a) An 800 nm pump laser pulse is normally incident from the Co layer side and the emitted THz signals are detected along the z axis with a transmission geometry. b) Magnetic hysteresis loops of the Co (3)/Mn<sub>2</sub>Au (5) and Co (3)/Mn<sub>2</sub>Au (8). The values in parentheses indicate the thickness of the layers in nanometers. c) The THz waveforms of Co/Mn<sub>2</sub>Au bilayers in comparison with ZnTe, Co, and Mn<sub>2</sub>Au single layers; Co/Pt and Mn<sub>2</sub>Au/Pt bilayers, obtained from the similar experimental conditions. Signals' strengths are scaled by the amounts for better comparability. d) Fourier-transformed spectra for Co/Mn<sub>2</sub>Au, Co/Pt, and ZnTe, which are normalized to peak amplitude 1.

collimated with the excitation laser spot (diameter of 4 mm) on the sample. Figure 1b shows the in-plane magnetic hysteresis loops of the Co (3)/Mn<sub>2</sub>Au (5) and Co (3)/Mn<sub>2</sub>Au (8), measured by a vibrating sample magnetometer. The inset (right below) shows an angular remanence magnetization (ARM) curve, the magnetization versus the field angle with respect to the *x* axis. The normalized ARM curve of the Co (3)/Mn<sub>2</sub>Au (5) exhibits a twofold symmetry with a small remanence ratio, indicating a relatively weak uniaxial magnetic anisotropy. The magnetization (**M**) of the Co/Mn<sub>2</sub>Au heterostructures was set by applying external magnetic field **H** = 2000 Oe (sufficient to saturate the Co film) parallel to the *x* axis. The forward-propagation high-frequency THz electric field, *E*(*t*), is inaccessible to the electrical measurement technique, but can be collected with electro-optical sampling (EOS) in the time domain, *E*<sub>THz</sub><sup>EOS</sup>(*t*) (see Experimental Section).

Before we proceed with the results of measurement and interpretation, we noted again the idea of our experiment. When the Co/AFM heterostructures are illuminated by femtosecond pumping pulses, a strongly out of equilibrium carrier distribution is easily created in the FM Co layer. On the one hand, the ultrafast demagnetization and coherent spin precession are often accompanied by the transient magnetic moment.<sup>[39,40]</sup> Such a response is analogous to a straightforward Hertzian dipole leading to a purely THz ultrafast magnetic dipole radiation (UMDR), *E*<sub>M</sub>(*t*).<sup>[41]</sup> On the other hand, during the excited hot carriers diffuse and relax, the majority-spin electrons are *sp*-like band electrons and persist for a longer time at high energies than the minority-spin electrons in *d* band,<sup>[35]</sup> resulting in an ultrafast spin-polarized current.<sup>[30,31]</sup> As the spin diffusion length of the Co layer (38 ± 12 nm) is much larger than the thickness of Co layer (3 nm),<sup>[42]</sup> the spin-polarized current **j**<sub>s</sub> can penetrate superdiffusively into the adjacent AFM layers. Based on the ISHE, **j**<sub>s</sub> can be converted into the charge current **j**<sub>c</sub>, due to the strong spin-orbit coupling of AFM layer. The efficiency of spin-charge interconversion can be quantified by the product of the spin Hall angle θ<sub>AFM</sub> and the spin diffusion length λ<sub>sd</sub>. In addition, the spin current injection efficiency should be material and interface dependent. In the direction orthogonal to both the **M** and **j**<sub>s</sub>, the transient **j**<sub>c</sub> flowing along the AFM layer is expected to generate THz emission, *E*<sub>P</sub>(*t*). The UMDR and the ISHE for THz radiation remain entangled with how an ultrafast laser pulse can modify the magnetic system. In terms of ISHE, the polarity of *E*<sub>P</sub>(*t*) changes sign when the sample is flipped about **M** (“odd” symmetry). In contrast, the sign of *E*<sub>M</sub>(*t*) does not change for the case of UMDR (“even” symmetry).

Upon photoexcitation by linear-polarized ultrafast optical pulses, as shown in Figure 1c, we detected the *E*<sub>THz</sub><sup>EOS</sup>(*t*) from Co (3)/Mn<sub>2</sub>Au (5) and Co (3)/Mn<sub>2</sub>Au (8) bilayers fabricated on MgO (100) substrate. *E*<sub>THz</sub><sup>EOS</sup>(*t*) was measured with pump fluence of 1.4 mJ/cm<sup>2</sup> and **H** = +2000 Oe applied along the *x* axis at room temperature. In the same figure, we compare the *E*<sub>THz</sub><sup>EOS</sup>(*t*) generated from a nominally identical 3 nm-thick Co single layer, a 5 nm-thick Mn<sub>2</sub>Au single layer, a Co (3)/Pt (3) bilayer, a Mn<sub>2</sub>Au (5)/Pt (7) bilayer, and a 1 mm-thick (110)-ZnTe, as reference samples. The THz emission from Co (3)/Mn<sub>2</sub>Au (5) has an amplitude ≈5% of that generated by a 1 mm-thick (110)-ZnTe crystal, and ≈12.5 % of that generated by an optimal Co (3)/Pt (3)

bilayer, which were measured under identical experimental conditions. Figure 1d shows the normalized frequency-domain spectra *E*<sub>THz</sub><sup>EOS</sup>(*f*) after Fourier transform of the time domain *E*<sub>THz</sub><sup>EOS</sup>(*t*) for Co (3)/Mn<sub>2</sub>Au (5), a mature nonlinear crystal ZnTe, and an optimized spintronic THz emitter Co (3)/Pt (3). In the covering frequency range of 0.1–3 THz, we observe that the bandwidth of *E*<sub>THz</sub><sup>EOS</sup>(*f*) from a 1 mm-thick ZnTe cover a wider range of frequencies, as compared with Co (3)/Mn<sub>2</sub>Au (5). The result suggests that the spectral bandwidth of our Co/Mn<sub>2</sub>Au bilayer is not limited by that of the THz detection crystal. The dynamic range of *E*<sub>THz</sub><sup>EOS</sup>(*t*) radiated from Co (3)/Mn<sub>2</sub>Au (5) is around 30 dB.

To better understand the origin of THz generation from Co/Mn<sub>2</sub>Au heterostructures, several control experiments have been carried out. First, the thickness of Co layer used in this work was chosen to be 3 nm, which ensures a virtually uniform pump intensity distribution within the Co film.<sup>[41]</sup> Thus, the effect related to hot electron diffusion within the Co film can be safely excluded. Second, the normal-incidence excitation scheme can greatly eliminate the contribution of magnetically enhanced surface nonlinearity to the THz emission.<sup>[43]</sup>

We further carry out the THz emission measurements by the following four geometrical arrangements, in which 1) inverting the magnetic field direction and 2) rotating the sign upon sample flip. As shown the schematics in Figure 2a, ❶ and ❷ indicate the pump pulse excites the heterostructure from Co layer side with **H** fixed parallel and antiparallel to the *x* axis, respectively. By turning the sample around, ❸ and ❹ indicate the pump pulse excites the sample from MgO substrate side with +**H** and –**H**, respectively. Figure 2b shows the *E*<sub>THz</sub><sup>EOS</sup>(*t*) from Co (3)/Mn<sub>2</sub>Au (5) with ❶–❹ four experimental geometries.

As the raw data shown in Figure 2b, change the direction of the magnetizing field (+**H** to –**H**) inverts the THz pulse, that is reversing the phase of the THz pulse. It confirms the spin-based origin of THz emission in the Co/Mn<sub>2</sub>Au heterostructure. The polarization of emitted THz pulses (along *z* axis) is always perpendicular to the **M** (along *x* axis). Compared the THz emission in the cases of ❶ and ❸ (❷ and ❹), the polarity of *E*<sub>THz</sub><sup>EOS</sup>(*t*) is found to be reverse sign. In addition, as shown in Figure 1c, the amplitude of THz radiation arising from Co/Mn<sub>2</sub>Au is significantly stronger than that from Co single layer with a same thicknesses of 3 nm. All observations are in agreement with the spin transport model.

Figure 2c shows the peak-to-peak value (*E*<sub>THz</sub><sup>peak</sup>) of the THz signal as a function of pump fluence for Co (3)/Mn<sub>2</sub>Au (5) and Co (3)/Pt (3). *E*<sub>THz</sub><sup>peak</sup> was defined as the difference between the amplitude maximum and minimum of the THz EOS signal. *E*<sub>THz</sub><sup>peak</sup> initially increases with an increase in the pump fluence, and then shows a saturating trend. The experimental data are well fitted by the saturation formula, with the best-fit saturation fluence *F*<sub>sat</sub> = 1.52 and 1.13 mJ/cm<sup>2</sup> for Co (3)/Mn<sub>2</sub>Au (5) and Co (3)/Pt (3), respectively.

To distinguish the THz generation mechanism of Co (3)/Mn<sub>2</sub>Au (5) from nonlinear optical effect, we investigate the azimuthal angle and pump polarization dependences of the THz generation.<sup>[44]</sup> Under the experimental geometry of ❶, Figure 2d shows the THz generation from Co (3)/Mn<sub>2</sub>Au (5) as a function of the sample azimuthal angle at a fixed pump

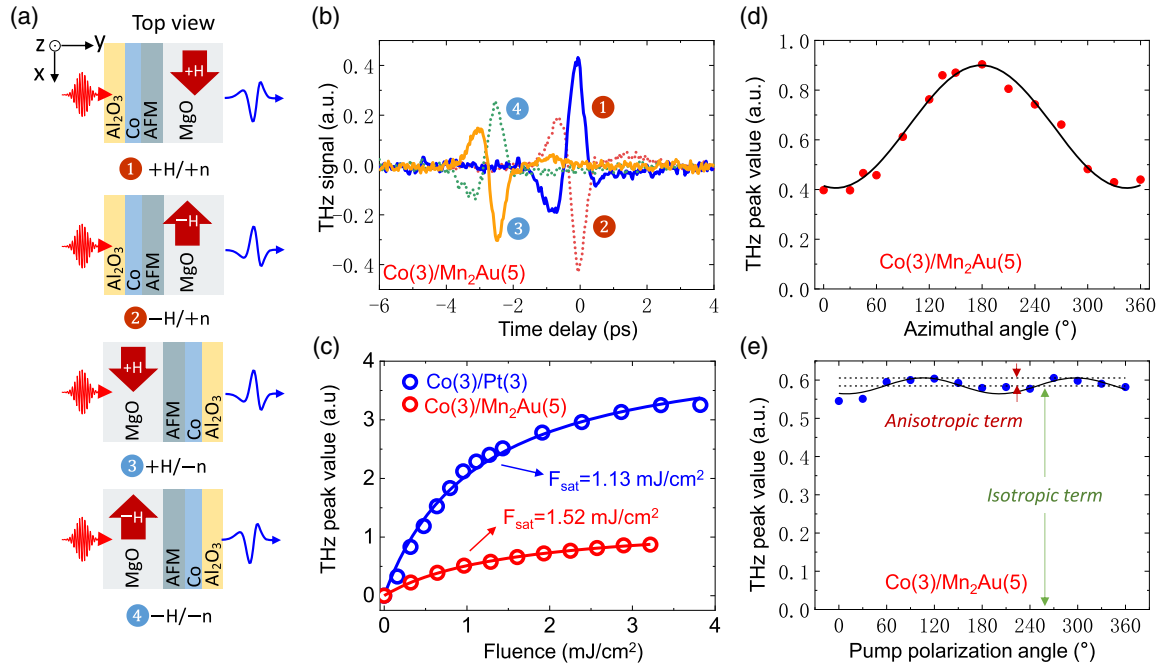


**Figure 2.** a) Schematics of the emitted THz radiation depends on the direction of the magnetic field (+H / -H) and layer directionality (+n / -n: the pump is incident from the side of AFM layer or the side of MgO substrate, respectively). b)  $E_{\text{THz}}^{\text{EOS}}(t)$  measured from Co (3)/Mn<sub>2</sub>Au (5) at room temperature with four experimental geometries. The zero-time delay corresponds to an arbitrary starting position. The time-delay between the cases of ① and ③ (② and ④) is due to the group velocity mismatch of 800 nm optical pulse and THz pulse propagating in the MgO substrate. c–e) THz peak values as functions of the pump fluence (c), the azimuthal angle (d), and the pump polarization angle (e).

polarization. The THz peak value shows a onefold dependence. Figure 2e shows the THz emission peak amplitude as a function of the linearly pump polarization angle, which can be fitted by a cosine function. The experimental result indicates that both isotropic term and anisotropic term contribute to the THz emission signal. However, the fitted results indicate the anisotropic and isotropic terms have 3.3% and 96.7% contributions to the THz peak amplitude, respectively. Therefore, the THz emission by the anisotropic optical rectification term is negligible, compared with the isotropic ISHE term.

To further verify the contribution of the inverse Faraday effect (IFE),<sup>[5,45]</sup> inverse spin-orbit torque effect (ISOT),<sup>[46]</sup> spin-dependent photogalvanic effect (SDPGE)<sup>[38,47]</sup> to the THz generation, the pump pulse helicity-dependent excitation are carried out. As shown in Figure 3a, by pumping the Co (3)/Mn<sub>2</sub>Au (5) with linearly polarized (LP), left circularly polarized (LCP), and right circularly polarized (RCP) pulses, the THz emission gives almost the same result. Figure 3b shows the 3D THz emission waveforms ( $E_z$  and  $E_x$  components) for LP, LCP, and RCP pumping. We found that  $E_x$  is much smaller than  $E_z$ . The electric field of  $E_x$  does not change sign upon reversal of the helicity. Our results indicate that ISHE is dominantly responsible for THz generation from the sample, and the contributions from ISOT and SDPGE are negligible.

We may also point out that based on the spin-charge conversion for THz emission, it is expected that both AFM/HM and AFM layers will produce negligible THz signal. As shown in Figure 1c, we do not observe any THz emission from Mn<sub>2</sub>Au/Pt bilayer and pure Mn<sub>2</sub>Au thin film, in which both

samples have zero net magnetization. This is consistent with the results obtained from IrMn/Pt bilayer.<sup>[48]</sup> Thus, we can further rule out the ultrafast demagnetization in the AFM layer as the possible THz emission mechanism.

As shown in Figure 1c, the Co (3)/Mn<sub>2</sub>Au (5) heterostructure shows around 2.37 times larger THz emission than that from Co (3)/Mn<sub>2</sub>Au (8) bilayer. As the sample thickness is much smaller than the wavelength of the THz radiation, the THz emissions can be understood by<sup>[31]</sup>

$$E_{\text{THz}}(\omega) = eZ(\omega)I_c \quad (1)$$

where  $e$  is the fundamental charge.  $Z(\omega)$  is the measured bilayer impedance, quantifying the efficiency of charge current to THz field conversion.  $Z(\omega) = \frac{Z_0}{n_1(\omega) + n_2(\omega) + Z_0 \int_0^{\text{tot}} \sigma(y, \omega) dy}$ , where  $n_1(\omega)$  and  $n_2(\omega)$  are the refractive indices of air and the MgO substrate, respectively. For simplicity, we ignore the frequency dependence,  $n_1 = 1$  and  $n_2 = 3.2$ .  $Z_0 = 377 \Omega$  is the impedance of vacuum.  $\sigma(y, \omega)$  is the in-plane conductivity of the Co/Mn<sub>2</sub>Au at depth  $y$ . Figure 4a,b shows the real ( $\sigma_1$ ) and imaginary ( $\sigma_2$ ) parts of the THz sheet conductivities for Co (3)/Mn<sub>2</sub>Au (5) and Co (3)/Mn<sub>2</sub>Au (8), respectively, measured by contact-free THz time domain spectroscopy (THz TDS, see Experimental Section). The complex sheet conductivity can be fitted well by a Drude-Smith model,  $\tilde{\sigma}_{\text{sheet}}(\omega) = \frac{\sigma_{\text{s,DC}}}{1 - i\omega\tau} [1 + \frac{c}{1 - i\omega\tau}]$ , where  $\sigma_{\text{s,DC}}$  is the sheet DC conductivity,  $\tau$  is the momentum scattering time,  $c$  (between -1 and 0) represents the localization degree of carrier's scattering. Drude-Smith model is used to fit the real and imaginary parts of

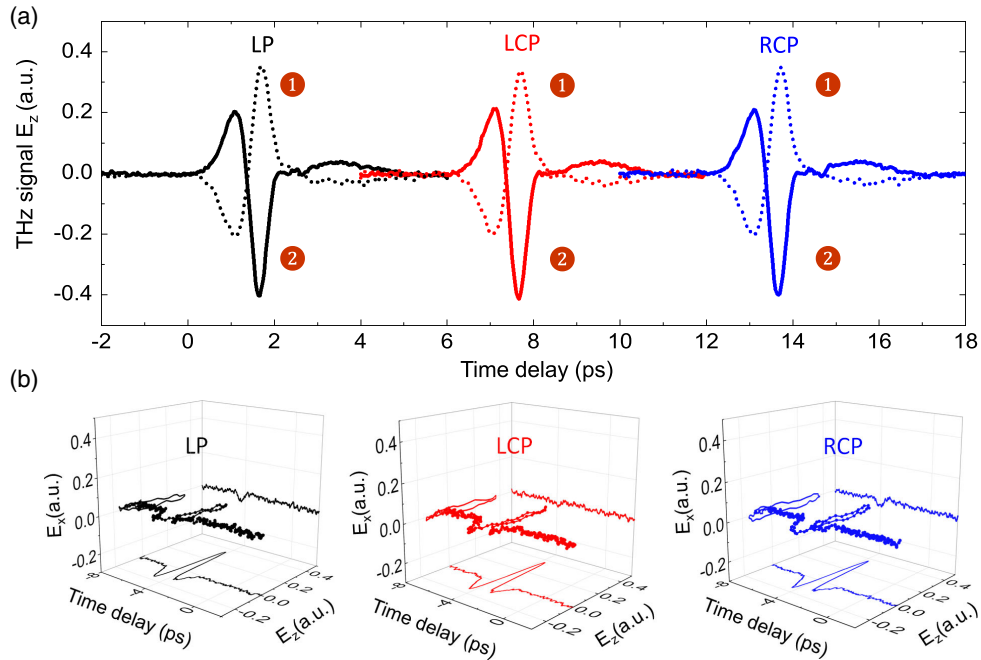


**Figure 3.** a) THz emission waveforms of Co (3)/Mn<sub>2</sub>Au (5) in the time domain at room temperature, measured for linearly polarized (LP) pump pulse and circularly polarized pump pulses with opposite helicities (RCP: right circularly and LCP: left circularly polarized pump pulses). The THz signals are shifted horizontally for clarity. b) The measured 3D temporal THz emission waveforms with LP, LCP, and RCP pumping.

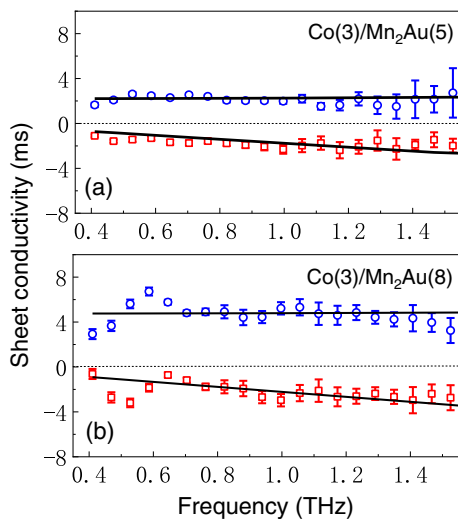


**Figure 4.** The real and imaginary parts of the complex conductivity spectra of a) Co (3)/Mn<sub>2</sub>Au (5) and b) Co (3)/Mn<sub>2</sub>Au (8) at room temperature. The Drude–Smith model fits are also plotted in the figures. The error bars are the standard deviations calculated from multiple measurements.

$\bar{\sigma}_{\text{sheet}}(\omega)$ , yielding the sheet DC conductance  $\sigma_{s,DC} = 2.2$  and 4.8 mS for Co (3)/Mn<sub>2</sub>Au (5) and Co (3)/Mn<sub>2</sub>Au(8), respectively.

In contrast, the in-plane sheet charge current  $I_c$  in the AFM layer can be described by,  $I_c \propto j_s^0 [T_{\text{FM}/\text{AFM}} \times \theta_{\text{AFM}} \times \lambda_{\text{sd}} \times \tanh(\frac{d_{\text{AFM}}}{2\lambda_{\text{sd}}})]$ , where  $j_s^0$  is the spin current density injected through the FM/AFM interface into the AFM layer. The factor  $T_{\text{FM}/\text{AFM}}$  represents the spin–angular-momentum transfer at FM/AFM interfaces.<sup>[49]</sup>

The spin Hall angle  $\theta_{\text{AFM}} = 0.035$  for Mn<sub>2</sub>Au.<sup>[28]</sup> The spatial distribution of  $j_s^0$  is determined by the spin diffusion length  $\lambda_{\text{sd}} = 1.6$  nm and the thickness of AFM layer  $d_{\text{AFM}}$ . We then calculate the ratio of  $\frac{E_{\text{THz}}(\text{Co}(3)/\text{Mn}_2\text{Au}(5))}{E_{\text{THz}}(\text{Co}(3)/\text{Mn}_2\text{Au}(8))} = 2.22$ , which is normalized by the saturation magnetization of two samples. Although the result shows a good correlation between the experimental ratio and analytical model. It should be noted that the interface factor  $T_{\text{FM}/\text{AFM}}$  plays an important role, which might be connected to the spin- and energy-dependent interfacial electron transmission,<sup>[50]</sup> crystalline mismatch and roughness at the interface,<sup>[51]</sup> and exchange coupling of the FM/AFM interface.<sup>[52]</sup>

Next, **Figure 5a** shows the temperature-dependent THz emission signals from the Co (3)/Mn<sub>2</sub>Au (5) bilayer. The sample was magnetized at 300 K in advance and cooled under zero magnetic field. **Figure 5b** shows a decreasing of  $E_{\text{THz}}^{\text{peak}}$  upon cooling the sample from 300 to 10 K. Subsequently,  $E_{\text{THz}}^{\text{peak}}$  recovers as the sample is heated back to room temperature. As the amplitude spectra shown in **Figure 5c**, the bandwidth of the THz pulse is almost constant with different temperatures. In contrast, at lower temperatures, both the reduction of phonon absorption in optical rectification crystals<sup>[53,54]</sup> and increase in mobility in photoconductive switches<sup>[55]</sup> contribute to the enhanced THz radiation.

Based on the aforementioned analytical model, in the exact same excitation configuration, the THz-wave amplitude depends on both in-plane  $\mathbf{M}$  and conductivity of the sample. To check whether the temperature dependence of  $E_{\text{THz}}^{\text{peak}}$  is due to the  $j_s^0$ , we measure the magnetization of Co (3)/Mn<sub>2</sub>Au (5) by quantum design superconducting quantum interference device (MPMS3) (see Experimental Section). In **Figure 5d**, we show a slight

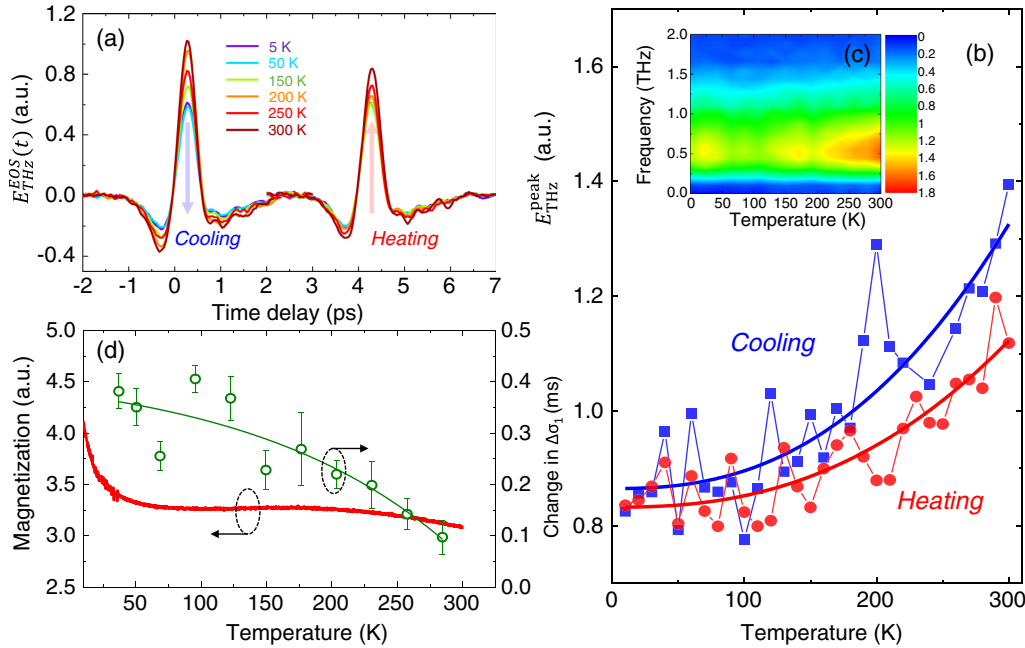


**Figure 5.** a) THz emission signal in time domain  $E_{\text{THz}}^{\text{EOS}}(t)$  measured at various temperatures from the Co (3)/Mn<sub>2</sub>Au (5) bilayer (+n and +H). The arrows represent the temperature direction for cooling and heating process, which are shifted horizontally. b)  $E_{\text{THz}}^{\text{peak}}$  as a function of temperature. The blue squares and red circles show the cooling and heating process, respectively. c) The corresponding temperature-dependent Fourier transform spectra. d) Left:  $M$ - $T$  curve of Co (3)/Mn<sub>2</sub>Au (5); Right: the temperature-induced change in the real part of sheet conductivity  $\Delta\sigma_1$ , calculated from the transmitted THz waveforms measured by THz-TDS.

increase in the  $\mathbf{M}$  as the sample is cooled, and reaching a plateau between 70 and 200 K.  $\mathbf{M}$  significantly increases below 70 K. This is consistent with previous observed temperature-dependent magnetization of Mn<sub>2</sub>Au.<sup>[56]</sup> Furthermore, previous study reported that the demagnetization dynamics are temperature independent for Co film.<sup>[57]</sup> Therefore, the temperature dependence of  $E_{\text{THz}}^{\text{peak}}$  cannot be simply explained in terms of the magnetization varied with temperature.

In contrast, we measured the transmitted THz waveforms through a 5 nm-thick Mn<sub>2</sub>Au layer by THz-TDS. Figure 5d shows the temperature-induced change in the real part of sheet conductivity  $\Delta\sigma_1$  (green circles), which indicates an general increasing trend of THz conductivity with decreasing temperature. The experimental results suggest that the metallic nature of the Mn<sub>2</sub>Au film and the negligible impurity contribution to the THz conductivity.<sup>[58]</sup> This experimental results reveal that the conductivity of Mn<sub>2</sub>Au plays an important role in the temperature dependence of THz emission. Our observation is basically consistent with recent reports on the temperature dependence of spin Hall resistivity of Pt layer.<sup>[57,59]</sup> We also would like to mention that with decreasing the temperature, the exchange coupling of FM/Mn<sub>2</sub>Au bilayer builds up, which was observed by an asymmetric shape of the hysteresis loops at low temperature.<sup>[52]</sup> A small modulation of the exchange-coupling strength at the interface between FM and AFM might lead to notable changes in magnetic properties. Therefore, further optical control of FM/AFM by optical/THz probing is highly intriguing, as the exchange-coupling torque in Fe/CoO heterostructure has been demonstrated at picosecond timescale.<sup>[60]</sup>

### 3. Conclusion

We have experimentally laser stimulated the THz emission from the Co/MnAu bilayer, using electro-optic sampling in the time domain. Our results are consistent with the explanation that light launches a spin current pulse into the AFM Mn<sub>2</sub>Au, wherein it interconverts into a radiative charge transient current due to the ISHE. It is found that Mn<sub>2</sub>Au is not a good spin current emitter, but an effective spin sink in THz emission. In addition, a general trend of THz amplitude decreases with decreasing the temperature is associated with the temperature-dependent conductivity of the Mn<sub>2</sub>Au layer. Our results demonstrate not only the sub-picosecond spin-charge interconversion in Co/Mn<sub>2</sub>Au heterostructures, but also a possibility of spectroscopic-based spin current detector at THz-frequency range.

### 4. Experimental Section

**Fabrication and Structure of the Co/Mn<sub>2</sub>Au Heterostructures:** The experiments were conducted in high-quality Co/Mn<sub>2</sub>Au heterostructures fabricated on the single crystal MgO (100) substrate. The 5 nm- and 8 nm-thick (103) oriented Mn<sub>2</sub>Au films were grown by magnetron sputtering at 573 K. The growth rate was 0.07 nm s<sup>-1</sup> and the base pressure was  $2.5 \times 10^{-5}$  Pa. A 3 nm-thick ferromagnetic Co layer was then grown on the top of the Mn<sub>2</sub>Au layer. The Co/Mn<sub>2</sub>Au heterostructure was finally covered by 1.5 nm Al, preventing the sample from oxidizing in the atmosphere.

**THz Emission Spectroscopy:** We excited the Co/Mn<sub>2</sub>Au bilayers with femtosecond optical pulses and measured the emitted THz radiation. The ultrafast laser beam (800 nm wavelength, 1 kHz repetition rate, diameter 4 mm, duration 120 fs) from a Ti:sapphire laser amplifier was irradiated on the sample with normal incidence. The magnetization direction of Co was aligned by an external magnetic field ( $\pm 2000$  Oe). We used a gate pulse (120 fs, 800 nm

laser pulses) that traveled along with the THz pulse in <110> ZnTe (1 mm thick) crystal. By using the balanced detection, the elliptical polarization impressed onto the gate beam by Pockels effect sampled the transient electric field of THz pulse, which was contact-free electro-optic sampling detection. Throughout the experiments, to guarantee comparable experimental conditions, the alignment of the THz spectroscopy and detector system were not changed during the exchange the samples. All experiments were carried out in the drying air environment. The absorbance, transmittance, and reflectance of pump beam for Co (3)/Mn<sub>2</sub>Au (5) were 2.7%, 62.6%, and 34.7%, respectively.

**THz Transmission Spectroscopy:** THz conductivity spectra of Co/Mn<sub>2</sub>Au were measured by a standard THz time-domain spectroscopy (THz-TDS). THz-TDS was driven by a mode-locked, centered wavelength at a 800 nm Ti:sapphire oscillator. The output beam was split into two laser beams, one was used to generate the THz pulse and the other was applied to detect the THz transient. The THz pulse produced by the photoconductive antenna focused on the sample by a polyethylene lens. The THz wave was collected by a detector antenna. The time-resolved THz signals could be detected by moving the optical delay. As the thicknesses of conducting films were much smaller than the wavelength and the skin depth, the thin conduction film approximation could be used to extract the complex conductivity,  $\frac{E_{\text{MgO}+\text{Co}/\text{AFM}}(\omega)}{E_{\text{MgO}}(\omega)} = \frac{1+n_{\text{MgO}}}{1+n_{\text{MgO}}+Z_0\sigma(\omega)d}$ , where  $Z_0 = \sqrt{\mu_0/\epsilon_0} = 377\Omega$  is the impedance of free space,  $d$  is the thickness of Co/AFM film, and the sheet conductivity  $\sigma_{\text{sheet}}(\omega) = \sigma(\omega)d$ . The refractive index of MgO,  $n_{\text{MgO}} \approx 3.2$ , was measured within 0.4–1.6 THz.

**Low-Temperature Magnetization Measurements:** The magnetization of Co (3)/Mn<sub>2</sub>Au (5) at different temperature was measured by the Quantum Design Superconducting Quantum Interference Device (MPMS3). The area of testing sample was about 1 mm<sup>2</sup>, fixed on the quartz rod by low-temperature glue. The magnetization along the surface of the sample was measured. First, the thin-film sample was premagnetized by applying a 2000 Oe magnetic field along the surface of the sample. Then, the magnetization of the sample was measured by 50 Oe probe magnetic field after removing the premagnetization magnetic field. The field-cooled cooling curve and the field-cooled warming curve of the sample overlapped with decreasing and increasing temperature.

## Acknowledgements

This work was supported by the National Natural Science Foundation of China (grant nos. 61988102, 61975110, 61735010, 51871130, and 61722111); the 111 Project (grant no. D18014); the Key Project supported by Science and Technology Commission of Shanghai Municipality (grant no. YDZX20193100004960). Science and Technology Commission of Shanghai Municipality (Shanghai Rising-Star Program grant no. 18QA1401700). Shanghai Educational Development Foundation (grant no. 16CG45). Young Chang Jiang Scholars Program and Beijing Innovation Center for Future Chip (ICFC).

## Conflict of Interest

The authors declare no conflict of interest.

## Keywords

bimetallic Mn alloys, inverse spin-Hall effects, spin-charge interconversion, THz conductivities, THz emission measurements

Received: May 30, 2021

Revised: June 23, 2021

Published online: August 2, 2021

- [1] T. Jungwirth, X. Marti, P. Wadley, J. Wunderlich, *Nat. Nanotechnol.* **2016**, *11*, 231.
- [2] V. Baltz, A. Manchon, M. Tsoi, T. Moriyama, T. Ono, Y. Tserkovnyak, *Rev. Mod. Phys.* **2018**, *90*, 015005.
- [3] A. Kirilyuk, A. Kimel, V., T. Rasing, *Rev. Mod. Phys.* **2010**, *82*, 2731.
- [4] T. Kampfrath, A. Sell, G. Klatt, A. Pashkin, S. Mahrlein, T. Dekorsy, M. Wolf, M. Fiebig, A. Leitenstorfer, R. Huber, *Nat. Photonics* **2011**, *5*, 31.
- [5] A. V. Kimel, A. Kirilyuk, P. A. Usachev, R. V. Pisarev, A. M. Balbashov, T. Rasing, *Nature* **2005**, *435*, 655.
- [6] S. Baierl, M. Hohenleutner, T. Kampfrath, A. K. Zvezdin, A. Kimel, V., R. Huber, R. V. Mikhaylovskiy, *Nat. Photonics* **2016**, *10*, 715.
- [7] P. Vaidya, S. A. Morley, J. V. Tol, Y. Liu, R. Cheng, A. Brataas, D. Lederman, E. D. Barco, *Science* **2020**, *368*, 160.
- [8] J. Li, C. B. Wilson, R. Cheng, M. Lohmann, M. Kavand, W. Yuan, M. Aldosary, N. Agladze, P. Wei, M. S. Sherwin, J. Shi, *Nature* **2020**, *578*, 70.
- [9] J. Sinova, S. O. Valenzuela, J. Wunderlich, C. H. Back, T. Jungwirth, *Rev. Mod. Phys.* **2015**, *87*, 1213.
- [10] H. Qiu, L. Zhou, C. Zhang, J. Wu, Y. Tian, S. Cheng, S. Mi, H. Zhao, Q. Zhang, D. Wu, B. Jin, J. Chen, P. Wu, *Nat. Phys.* **2021**, *17*, 388.
- [11] J. Železný, P. Wadley, K. Olejník, A. Hoffmann, H. Ohno, *Nat. Phys.* **2018**, *14*, 220.
- [12] P. Němec, M. Fiebig, T. Kampfrath, A. V. Kimel, *Nat. Phys.* **2018**, *14*, 229.
- [13] X. Chen, X. Zhou, R. Cheng, C. Song, J. Zhang, Y. Wu, Y. Ba, H. Li, Y. Sun, Y. You, Y. Zhao, F. Pan, *Nat. Mater.* **2019**, *18*, 931.
- [14] K. Olejník, T. Seifert, Z. Kašpar, V. Novák, P. Wadley, R. P. Campion, M. Baumgartner, P. Gambardella, P. Němec, J. Wunderlich, J. Sinova, P. Kužel, M. Müller, T. Kampfrath, T. Jungwirth, *Sci. Adv.* **2018**, *4*, 3566.
- [15] P. Wadley, B. Howells, J. Železný, C. Andrews, V. Hills, R. P. Campion, V. Novák, K. Olejník, F. Maccherozzi, S. S. Dhesi, S. Y. Martin, T. Wagner, J. Wunderlich, F. Freimuth, Y. Mokrousov, J. Kuneš, J. S. Chauhan, M. J. Grzybowski, A. W. Rushforth, K. W. Edmonds, B. L. Gallagher, T. Jungwirth, *Science* **2016**, *351*, 587.
- [16] H. Chen, Q. Niu, MacDonald, A. H. Anomalous, *Phys. Rev. Lett.* **2014**, *112*, 017205.
- [17] H. Tsai, T. Higo, K. Kondou, T. Nomoto, A. Sakai, A. Kobayashi, T. Nakano, K. Yakushiji, R. Arita, S. Miwa, Y. Otani, S. Nakatsuji, *Nature* **2020**, *580*, 608.
- [18] W. Zhang, W. Han, S.-H. Yang, Y. Sun, Y. Zhang, B. Yan, S. S. P. Parkin, *Sci. Adv.* **2016**, *2*, e1600759.
- [19] W. Zhang, M. B. Jungfleisch, W. Jiang, J. E. Pearson, A. Hoffmann, F. Freimuth, Y. Mokrousov, *Phys. Rev. Lett.* **2014**, *113*, 196602.
- [20] W. Feng, G. Guo, J. Zhou, Y. Yao, Q. Niu, *Phys. Rev. B* **2015**, *92*, 144426.
- [21] S. van Dijken, M. Besnier, J. Moritz, J. M. D. Coey, *J. Appl. Phys.* **2005**, *97*, 10K114.
- [22] A. Kohn, A. Kovács, R. Fan, G. J. McIntyre, R. C. C. Ward, J. P. Goff, *Sci. Rep.* **2013**, *3*, 2412.
- [23] S. Y. Bodnar, L. Šmejkal, I. Turek, T. Jungwirth, O. Gomonay, J. Sinova, A. A. Sapozhnik, H.-J. Elmers, M. Kläui, M. Jourdan, *Nat. Commun.* **2018**, *9*, 348.
- [24] A. A. Sapozhnik, R. Abrudan, Y. Skourski, M. Jourdan, H. Zabel, M. Kläui, H.-J. Elmers, *Phys. Status Solidi RRL* **2017**, *11*, 1600438.
- [25] X. Zhou, J. Zhang, F. Li, X. Chen, G. Shi, Y. Tan, Y. Gu, M. S. Saleem, H. Wu, F. Pan, C. Song, *Phys. Rev. Appl.* **2018**, *9*, 054028.
- [26] X. Zhou, X. Chen, J. Zhang, F. Li, G. Shi, Y. Sun, M. S. Saleem, Y. You, F. Pan, C. Song, *Phys. Rev. Appl.* **2019**, *11*, 054030.
- [27] J. B. S. Mendes, R. O. Cunha, O. A. Santos, P. R. T. Ribeiro, F. L. A. Machado, R. L. Rodríguez-Suárez, A. Azevedo, S. M. Rezende, *Phys. Rev. B* **2014**, *89*, 140406.

- [28] M. Arana, M. Gamino, E. F. Silva, V. M. T. S. Barthem, D. Givord, A. Azevedo, S. M. Rezende, *Phys. Rev. B* **2018**, *98*, 144431.
- [29] E. Saitoh, M. Ueda, H. Miyajima, G. Tatara, *Appl. Phys. Lett.* **2006**, *88*, 182509.
- [30] K. Uchida, M. Ishida, T. Kikkawa, A. Kirihara, T. Murakami, E. Saitoh, *J. Phys.: Condens. Matter* **2014**, *26*, 389601.
- [31] T. Kampfrath, M. Battiato, P. Maldonado, G. Eilers, J. Nötzold, S. Mährlein, V. Zbarsky, F. Freimuth, Y. Mokrousov, S. Blügel, M. Wolf, I. Radu, P. M. Oppeneer, M. Münzenberg, *Nat. Nanotechnol.* **2013**, *8*, 256.
- [32] T. Seifert, S. Jaiswal, U. Martens, J. Hannegan, L. Braun, P. Maldonado, F. Freimuth, A. Kronenberg, J. Henrizi, I. Radu, E. Beaurepaire, Y. Mokrousov, P. M. Oppeneer, M. Jourdan, G. Jakob, D. Turchinovich, L. M. Hayden, M. Wolf, M. Münzenberg, M. Kläui, T. Kampfrath, *Nat. Photonics* **2016**, *10*, 483.
- [33] T. S. Seifert, S. Jaiswal, J. Barker, S. T. Weber, I. Razzdolski, J. Cramer, O. Gueckstock, S. F. Maehrlein, L. Nadvornik, S. Watanabe, C. Ciccarelli, A. Melnikov, G. Jakob, M. Münzenberg, S. T. B. Goennenwein, G. Woltersdorf, B. Rethfeld, P. W. Brouwer, M. Wolf, M. Kläui, T. Kampfrath, *Nat. Commun.* **2018**, *9*, 2899.
- [34] D. Yang, J. Liang, C. Zhou, L. Sun, R. Zheng, S. Luo, Y. Wu, J. Qi, *Adv. Opt. Mater.* **2016**, *4*, 1944.
- [35] L. Cheng, X. Wang, W. Yang, J. Chai, M. Yang, M. Chen, Y. Wu, X. Chen, D. Chi, K. E. J. Goh, J. Zhu, H. Sun, S. Wang, J. C. W. Song, M. Battiato, H. Yang, E. E. M. Chia, *Nat. Phys.* **2019**, *15*, 347.
- [36] X. Wang, L. Cheng, D. Zhu, Y. Wu, M. Chen, Y. Wang, D. Zhao, C. B. Boothroyd, Y. M. Lam, J. Zhu, M. Battiato, J. C. W. Song, H. Yang, E. E. M. Chia, *Adv. Mater.* **2018**, *30*, 1802356.
- [37] M. Tong, Y. Hu, Z. Wang, T. Zhou, X. Xie, X. Cheng, T. Jiang, *Nano Lett.* **2021**, *21*, 60.
- [38] X. Chen, H. Wang, C. Wang, C. Ouyang, G. Wei, T. Nie, W. Zhao, J. Miao, Y. Li, L. Wang, X. Wu, *Adv. Photonics Res.* **2021**, *2*, 2000099.
- [39] J.-Y. Bigot, M. Vomir, E. Beaurepaire, *Nat. Phys.* **2009**, *5*, 513.
- [40] E. Beaurepaire, G. M. Turner, S. M. Harrel, M. C. Beard, Y. Bigot, C. A. Schmuttenmaer, *Appl. Phys. Lett.* **2004**, *84*, 3465.
- [41] W. Zhang, P. Maldonado, Z. Jin, T. S. Seifert, J. Arabski, G. Schmerber, E. Beaurepaire, M. Bonn, T. Kampfrath, P. M. Oppeneer, D. Turchinovich, *Nat. Commun.* **2020**, *11*, 4247.
- [42] L. Piraux, S. Dubois, A. Fert, L. Belliard, *Eur. Phys. J. B* **1998**, *4*, 413.
- [43] D. J. Hilton, R. D. Averitt, C. A. Meserole, G. L. Fisher, D. J. Funk, J. D. Thompson, A. J. Taylor, *Opt. Lett.* **2004**, *29*, 1805.
- [44] Z. Yao, H. Fu, W. Du, Y. Huang, Z. Lei, C. You, X. Xu, *Phys. Rev. B* **2021**, *103*, L201404.
- [45] R. Hertel, *J. Magn. Magn. Mater.* **2006**, *303*, L1.
- [46] T. Huisman, R. Mikhaylovskiy, J. Costa, F. Freimuth, E. Paz, J. Ventura, P. Freitas, S. Blügel, Y. Mokrousov, T. Rasing, A. Kimel, *Nat. Nanotechnol.* **2016**, *11*, 455.
- [47] X. Tao, P. Jiang, H. Hao, X. Zheng, L. Zhang, Z. Zeng, *Phys. Rev. B* **2020**, *102*, 081402.
- [48] M. Chen, R. Mishra, Y. Wu, K. Lee, H. Yang, *Adv. Opt. Mater.* **2018**, *6*, 1800430.
- [49] G. Malinowski, F. Dalla Longa, J. H. H. Rietjens, P. V. Paluskar, R. Huijink, H. J. M. Swagten, B. Koopmans, *Nat. Phys.* **2008**, *4*, 855.
- [50] T. H. Dang, J. Hawecker, E. Rongione, G. Baez Flores, D. Q. To, J. C. Rojas-Sanchez, H. Nong, J. Mangeney, J. Tignon, F. Godel, S. Collin, P. Seneor, M. Bibes, A. Fert, M. Anane, J.-M. George, L. Vila, M. Cosset-Cheneau, D. Dolfi, R. Lebrun, P. Bortolotti, K. Belashchenko, S. Dhillon, H. Jaffrès, *Appl. Phys. Rev.* **2020**, *7*, 041409.
- [51] D. Nenno, L. Scheuer, D. Sokoluk, S. Keller, G. Torosyan, A. Brodyanski, J. Lösch, M. Battiato, M. Rahm, R. Binder, H. Schneider, R. Beigang, E. Papaioannou, *Sci. Rep.* **2019**, *9*, 13348.
- [52] A. A. Sapozhnik, M. Jourdan, H. Zabel, M. Kläui, H.-J. Elmers, *J. Phys. D: Appl. Phys.* **2019**, *52*, 465003.
- [53] M. Schall, P. Jepsen, *Appl. Phys. Lett.* **2000**, *77*, 2801.
- [54] X. Wu, C. Zhou, W. Huang, F. Ahr, F. Kärtner, *Opt. Express* **2015**, *23*, 29729.
- [55] B. Hu, X. Zhang, D. Auston, *Appl. Phys. Lett.* **1990**, *57*, 2629.
- [56] V. Barthem, C. Colin, H. Mayaffre, M. Julien, D. Givord, *Nat. Commun.* **2013**, *4*, 1.
- [57] M. Matthiesen, D. Afanasiev, J. Hortensius, T. Thiel, R. Medapalli, E. Fullerton, A. Caviglia, *Appl. Phys. Lett.* **2020**, *116*, 212405.
- [58] Z. Jin, S. Ruan, X. Zhou, B. Song, C. Song, X. Chen, F. Pan, Y. Peng, C. Zhang, G. Ma, Y. Zhu, S. Zhuang, *Phys. Rev. B* **2020**, *102*, 014438.
- [59] Y. Sasaki, G. Li, T. Moriyama, T. Ono, R. Mikhaylovskiy, A. Kimel, S. Mizukami, *Appl. Phys. Lett.* **2020**, *117*, 192403.
- [60] X. Ma, F. Fang, Q. Li, J. Zhu, Y. Yang, Y. Z. Wu, H. B. Zhao, G. Lüpke, *Nat. Commun.* **2015**, *6*, 8800.